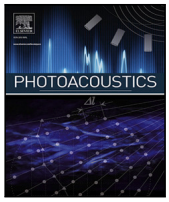
Photoacoustics 34 (2023) 100576



Contents lists available at ScienceDirect

Photoacoustics

journal homepage: www.elsevier.com/locate/pacs



Spatial resolution and reconstructed size accuracy using advanced beamformers in linear array-based PAT systems

Irene Pi-Martín, Alejandro Cebrecos *, Juan J. García-Garrigós, Noé Jiménez, Francisco Camarena

Instituto de Instrumentación para Imagen Molecular (i3M), CSIC – Universitat Politècnica de València, Camino de Vera S/N, 46022, Valencia, Spain

ARTICLE INFO

Keywords:
Photoacoustic imaging
Advanced beamformers
Full-Width-at-Half-Maximum (FWHM)
Point Spread Function (PSF)
Rayleigh criterion
Coherent radiation

ABSTRACT

Limitations associated with linear-array probes in photoacoustic tomography are partially compensated by using advanced beamformers that exploit the temporal and spatial coherence of the recorded signals, such as Delay Multiply and Sum (DMAS), Minimum Variance (MV) or coherence factor (CF), among others. However, their associated signal processing leads to an overestimation of the spatial resolution, as well as alterations in the reconstructed object size. Numerical and experimental results reported here support this hypothesis. First, we show that the Rayleigh criterion (RC) is the most suitable choice to characterize the spatial resolution instead of the Point Spread Function (PSF) when considering advanced beamformers. Then, we observe that several advanced beamformers fail to properly reconstruct target sizes slightly above the spatial resolution, underestimating their size. This work sheds light on the suitability of this type of beamformers combined with linear probes for determining sizes and morphology in photoacoustic images.

1. Introduction

Photoacoustic (PA) imaging can be used to study size, shape and molecular components of different biological structures [1]. It is widely used to characterize the morphology of surface vasculature [2], as to diagnose tumour diseases when the virulence or size of tumours is related to the vascularization generated around the tumour [3,4]. In addition, it is used to analyse cell size and structure, as the generated PA signal varies according to the cell internal structure. It has also been used to detect morphological changes resulting from photothermal treatments [5]. Therefore, a good resolution and accuracy of size and shape in the reconstructed images is key for applications where morphological analysis is of interest. An optimal reconstruction is achieved if sensors completely surround the sample to be imaged, as wavefronts with broadband angular spectrum can be fully captured [6–8]. However, if some angular components are lost, resolution is worsened and the stable reconstruction area is reduced [9].

Linear array ultrasound probes are widely used in photoacoustic tomography (PAT) due to its wide availability, low cost and versatility as compared to more complex sensor geometries [10–14]. However, their limited angular spectrum reduces the quality of the reconstructed images, creating unstable reconstruction regions [9] resulting in different resolutions for the lateral and axial directions [15]. To mitigate these limitations, advanced algorithms have been proposed, such as time-based [16–18], frequency-based [19,20] or pixel-based algorithms as Delay Multiply and Sum (DMAS) [21], Minimum Variance (MV) [22], MV-DMAS [23] or CF [24,25], among others. These algorithms use the spatial and temporal coherence properties of the PA signals to improve image properties such as the signal-to-noise-ratio (SNR) or the spatial resolution. However, their associated signal processing may lead to alterations on the size or morphology of the reconstructed PA absorbers, which is particularly relevant in applications where the morphology of the imaged targets is of interest.

The most common approach to characterize the spatial resolution of PAT systems is to reconstruct an image of a point target, mapping the combined effect of the physical process, excitation and acquisition systems, and the reconstruction method [26]. This map is the Point Spread Function (PSF) and its Full-Width-at-Half Maximum (FWHM) is the spatial resolution. However, for the classical definition of resolution following the Rayleigh criterion (RC), i.e., the minimum distance between two distinct objects that can be distinguished as separate entities, two objects separated at different distances should be analysed. This might be particularly relevant for advanced beamformers, which are very effective in exploiting the temporal and spatial coherence of the recorded signals coming from multiple scatterers, but they may introduce artefacts [27] and alterations on the spatial resolution of the reconstructed images [28].

Some of the existing methods to characterize the spatial resolution have been adapted to ultrasound and photoacoustic imaging from

* Corresponding author.
E-mail address: alcebrui@upv.es (A. Cebrecos).

https://doi.org/10.1016/j.pacs.2023.100576
Received 22 June 2023; Received in revised form 14 November 2023; Accepted 27 November 2023
Available online 29 November 2023
2213-5979/© 2023 The Authors. Published by Elsevier GmbH. This is an open access article under the CC BY-NC-ND license (http://creativecommons.org/licenses/by-nc-nd/4.0/).

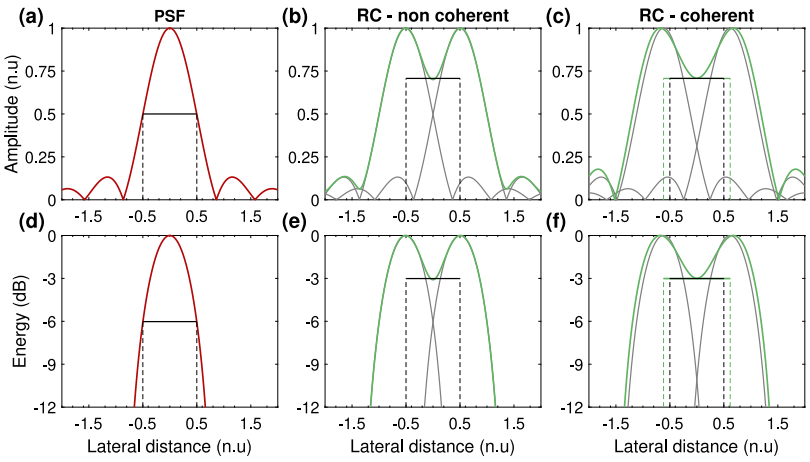


Fig. 1. Analytical comparison of lateral resolution from an Airy disc pattern using the FWHM of the PSF and RC. Non-coherent and coherent radiation are considered.

optical systems such as telescopes or microscopes, where waves exhibit an Airy diffraction pattern in the far-field due to Fraunhofer diffraction, and the considered radiation is non-coherent [29]. However, ultrasound waves from two separate sources interact coherently, which prompts differences when estimating the resolution using a single source (PSF) or two closely-spaced ones (RC). To illustrate this, as shown in Fig. 1, an Airy pattern has been considered, with amplitude $A = 2J_1(\sqrt{2}\pi x)/(\sqrt{2}\pi x)$, where J_1 is a Bessel function of the first kind and the factor $\sqrt{2}$ accounts for the FWHM in acoustic amplitude [15]. The −6 dB FWHM of the PSF in Fig. 1(a, d) and the −3 dB dip in the interference pattern of two closely-spaced sources (RC) in Fig. 1(b, e), coincide for non-coherent radiation. However, if coherent radiation is considered, as shown in Fig. 1(c, f), the obtained source separation to fulfil the RC is increased by a factor 1.235. Hence, this factor should be accounted for when reporting the resolution in ultrasound or photoacoustic imaging systems.

In this work, we numerically and experimentally study how resolution and object size is affected in a linear array-based PA imaging system if advanced beamformers are applied. First, the spatial resolution is determined through the PSF of a single source. Then, the resolution is evaluated using the RC. Results using both methods are compared, obtaining an overestimated resolution when applying the PSF method to images reconstructed using advanced algorithms. Furthermore, advanced beamformers are used to compare the PA reconstructed size of different targets with respect to their actual sizes, showing how some of these beamformers underestimate the size of targets which are similar and slightly larger than the system resolution.

This paper is structured as follows, Section 2 describes the tools used, and the procedures followed for the two types of evaluation tests, first, to determine the system resolution and, afterwards, to study the size reconstruction accuracy. Section 3 shows and discusses the main results of the two proposed evaluation tests. And, finally, Section 4 presents the concluding remarks.

2. Materials and methods

Target sources of increasing size has been used to evaluate the spatial resolution and accuracy of their reconstructed images with several beamformers. In both cases, numerical simulations and experiments have been carried out and results have been compared.

2.1. Lateral and axial resolution

Theoretical expressions of the lateral and axial resolutions in an acoustically-resolved PA system, which are respectively labelled as R_L and R_A, are defined by [30]

$$R_L = 0.71 \cdot \frac{c_0}{\mathrm{NA} \cdot f_0}, \tag{1}$$

$$R_A = 0.88 \cdot \frac{c_0}{\Delta f}, \tag{2}$$

where c_0 is the sound speed in the medium, NA is the acoustic numerical aperture, f_0 is the PA central frequency and Δf is the PA signal bandwidth. The bandwidth is presumed to be proportional to f_0, and it is normally determined by factors as the laser pulse width, the depth of the object, the attenuation of the medium and the bandwidth of the transducer itself [30]. However, since the PA signal bandwidth is usually much broader than that of the sensor, especially when using piezoelectric transducers, both f_0 and Δf are ultimately given by the detector frequency response. Note that these expressions are closely related to the PSF method, since they are defined as the corresponding FWHM of the system response to a point target, i.e., a target much smaller than the resolution of the imaging system.

Empirically, the resolution has been determined using two methods, as shown in Fig. 2. First, we obtain the PSF of an individual point source, i.e., the PA image of an object much smaller than the acoustic wavelength. In this method, the system resolution is measured as the FWHM of the reconstructed profile (Figs. 2(a-b)). Second, two close objects are imaged, and the resolution is thus determined according to the RC method, (Fig. 2(c-d)), by reconstructing the PA images of two point sources with the algorithms under test. As shown in Fig. 2(d), the profile present two peaks corresponding to each source, and a valley between them as the local minimum of the profile. The system resolution for the RC method is then defined as the smallest distance between peaks at which the peak-to-valley difference (PV) is greater than 3 dB, so that the two PA sources are resolved as independent.

2.2. Size evaluation

In a second experiment, PA sources of growing size have been measured in order to find out how accurate each of the algorithms are when reconstructing target object sizes, and also whether this accuracy varies with their size. In this way, target sources with a square cross-section and different sizes have been chosen to ensure that their top and bottom sides are reconstructed in a stable way [9], and also to properly measure their actual size in the PA image. Fig. 3(a) shows a representation of the experimental configuration for this study. In the reconstruction, a threshold of 70% of the signal-to-background level has been defined on the stable (top and bottom) faces profiles in order to measure the size of the piece, as illustrated in Fig. 3(b). This threshold value was set using the largest pieces, where both classical and advanced algorithms were applied to obtain the target size in the PA image.

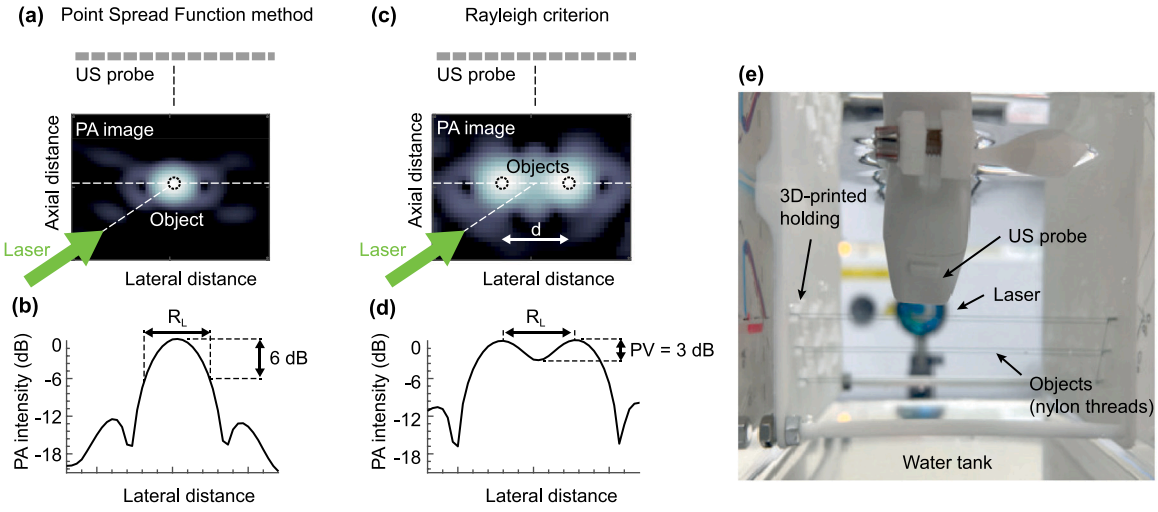


Fig. 2. Experimental configuration to measure the spatial resolution using (a–b) the point-spread-function (PSF) method and (c–d) the Rayleigh criterion (RC). (a) Schematic and example of a PA reconstructed image using a single object for the PSF method. (b) Transverse profile of the PSF and FWHM estimation. (c) Corresponding schematic for the RC method using a pair of closely-located objects. (d) Transverse profile and peak-to-valley (PV) distance estimation. (e) Photograph of the experimental setup.

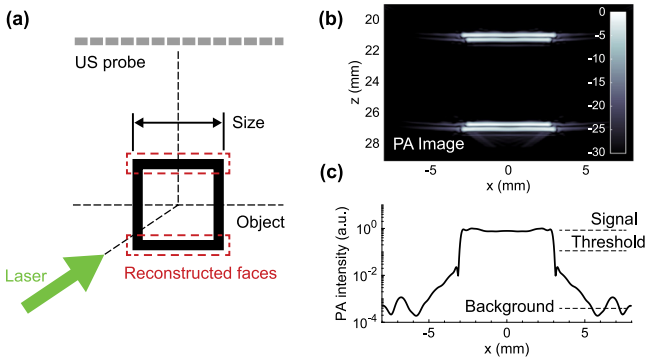


Fig. 3. Experimental configuration to evaluate the reconstructed size. (a) Schematic of the experimental setup. (b) PA image showing the top and bottom edges of the target. (c) Description of the post-processing used for size estimation. Continuous black line corresponds to the horizontal profile of the bottom edge of the PA source, black dashed lines indicate the signal and background levels, as well as the threshold.

2.3. Experimental setup

The PAT system used in this work consist of an EKSPLA Optical Parametric Oscillator (OPO) laser tuned at 532 nm optical wavelength, and a Verasonics Vantage 256™ ultrasound acquisition platform connected to a 128-elements L11-5v Verasonics linear probe with a NA = 0.606, central frequency f_0 = 7.6 MHz and 77% bandwidth. The OPO delivered a collimated laser beam to excite the samples with a cross-section diameter of 15 mm (after expanding the beam by a factor of 3), 10 Hz pulse repetition rate, 6 ns pulse duration and a pulse energy of 30 mJ, having a fluence below the safety limit [31]. The synchronization between the laser pulse excitation and the ultrasound acquisition system was controlled by the Verasonics Vantage 256™ triggering system.

The PA targets used for the resolution study were 0.1 mm diameter black nylon threads placed at 25 mm distance from the probe, as shown in Fig. 2(b). On the other hand, for the size accuracy evaluation study, hollow square pieces were 3D-printed, using side sizes ranging from 1 mm to 15 mm. Tough 2000 Formlabs photosensitive resin was used, and squares were arranged with their sides parallel to the probe, as shown in Fig. 3(a). In both setups, samples were immersed in deionized water and positioned to ensure direct illumination of two perpendicular faces.

2.4. Numerical simulations

Numerical 3D simulations have been carried out for both studies using a pseudo-spectral time-domain method using the k-Wave toolbox [32]. A volume of $50.7 \times 50.7 \times 50.97$ mm has been simulated with a voxel size of 25 μm. The geometry of the Verasonics L11-5v (width, length, kerf) has been considered to define the US probe, as well as its frequency response and directivity.

The full 3D shape and size of the objects used experimentally have been simulated. PA emitters have been considered ideal in terms of emission and directivity. In addition, for the size evaluation study, the numerical analysis has been extended to smaller sizes than in experiments, considering solid sources from 0.1 mm to 1 mm cross-section.

2.5. Beamforming algorithms

Multiple pixel-based PAT image reconstruction algorithms have been implemented and compared in this work, considering linear and non-linear as well as non-adaptive and adaptive types, namely: Delay and Sum (DAS) [33], Coherence Factor (CF) [25], Delay Multiply And Sum (DMAS) [21,34,35], Minimum Variance (MV) [22] and MV-DMAS [23]. The DAS algorithm is the classic beamformer for ultrasound imaging, which is linear and non-adaptive and has been modified for PAT by taking into account the arrival times only. CF uses phase information rather than amplitude to weight the PA received signals, having the effect of decreasing the secondary lobes. DMAS is a non-linear algorithm that multiplies the received signals from each channel in a combinatorial way, before performing the delay and sum, improving the SNR of the reconstructed images [21]. MV-based algorithms belong to the adaptive type and can be linear or non-linear, depending on the base beamformer from which they are built, typically DAS or DMAS. They estimate the covariance matrix using the recorded signals to calculate the optimal weight applied for each pixel and channel, which results in a greatly improved SNR and spatial resolution of the reconstructed images [22]. Particularly, MV has been implemented using spatial windows of $L = M/2$ and $L = M/4$ and the combined algorithm MV-DMAS with a window of $L = M/4$, where L is the size of the elements window considered for the calculation of the covariance matrices, and M is the total number of elements of the probe. It is worth noting that larger windows improve the resolution albeit at the cost of loss of robustness, and also that they should not exceed $M/2$ [36].

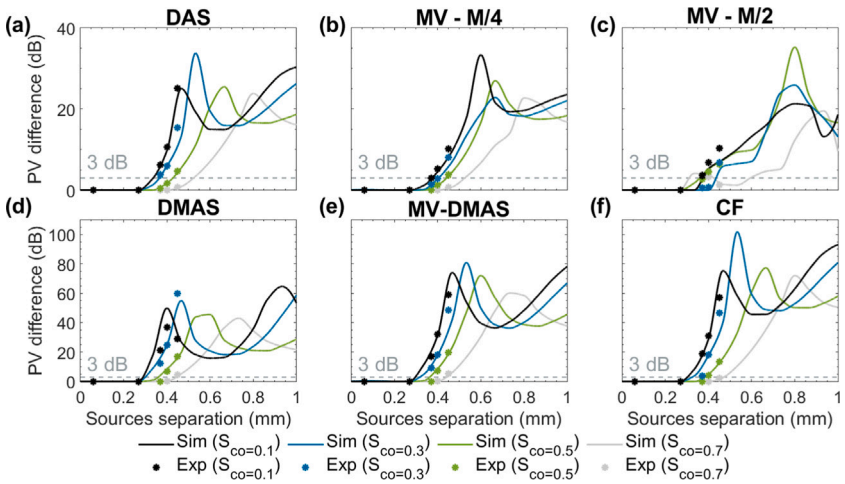


Fig. 4. Evolution of PV with the distance between sources on the lateral axis. Results obtained using the different algorithms implemented are represented from (a) to (f). The 3-dB threshold of the PV difference defining the RC lateral resolution is plotted with a grey dashed line.

For all the implemented algorithms, and for both numerical simulations and experiments, the influence of the so-called sensitivity cut-off parameter, S_{co}, has been considered. Its value, ranging from 0 to 1, corresponds to the amplitude of the normalized angular response of the detector at a certain angle. This parameter restricts the reception angle of each channel of the detector, reducing off-axis contributions. In this regard, if a given pixel-channel angle is larger than the one corresponding to S_{co}, the signal of that channel will be discarded during the beamforming process. The following sensitivity cut-off values, $S_{co} =$ 0.1, 0.3, 0.5, 0.7, have been considered.

3. Results and discussion

3.1. Lateral and axial resolution

The theoretical lateral and axial resolutions have been calculated using Eqs. (1), (2), yielding $R_L = 231$ μm and $R_A = 226$ μm, respectively. It should be noted that these expressions are not taking into account the kerf of the probe, i.e., the spacing between piezoelectric elements.

To obtain the resolution using the RC method, the PV difference (in dB) for each source separation distance is evaluated. The lateral and axial PV difference are shown in Figs. 4 and 5, respectively. A 3-dB threshold is set to the PV difference to obtain the resolution given by the RC method for each algorithm. A piecewise cubic hermite interpolating polynomial was used for interpolation of numerical and experimental data to determine the 3-dB threshold line. The PV difference gradually increases with source separation along the range measured experimentally, i.e., from 0.06 to 0.45 mm, showing a good agreement between simulated and experimental data. As the separation distance between targets increases further, oscillations in the PV difference arise, caused by the interaction between sources and especially due to the presence of side-lobes. For all algorithms, the first maximum takes place when the minimum of both PSFs between the main-lobe and the first side-lobe coincide. The first local minimum appears at a separation where the side-lobes interact constructively at their maximum. The amplitude of the oscillations depend on the main-lobe amplitude as well as its difference to the side-lobes, while the oscillation period is determined by the width of the side-lobes. For instance, MV-based algorithms tend to widen the side-lobes, resulting in a larger period of the PV oscillation than DMAS or CF, which originate thinner side-lobes, resulting in a smaller period.

The influence of the sensitivity cut-off (S_{co}) on the resolution is also shown in Figs. 4 and 5. As the value of the sensitivity cut-off increases fewer received angles are considered, effectively reducing the NA and hence, worsening the lateral resolution, as expected from Eq. (1). On the other hand, this phenomenon is not observed when calculating the axial resolution, since both sources are centred on the axis of the probe and the axial resolution does not depend on the NA, according to Eq. (2).

The lateral and axial resolutions obtained for each algorithm and method are shown in Figs. 6 and 7, respectively, using $S_{co} = 0.1$ for both methods. The theoretical lateral (R_L) and axial (R_A) resolutions are also included using black dashed lines. A good agreement is found between simulations and experiments. First, for the linear and non-adaptive beamformer (DAS), RC estimates a lateral resolution 25% larger than the PSF, a result matching the theoretical prediction for the RC coherent case, as highlighted in Fig. 1. Moreover, experimental and simulated resolution values of the PSF are slightly larger than the theoretical predictions from Eq. (1), due to the size of the photoacoustic source (0.1 mm diameter) failing to behave as an ideal point source.

If advanced beamformers are employed, dramatic differences are found between the two methods. While advanced beamformers allow to strongly improve the identification of single sources, showing a PSF-lateral resolution much smaller than the standard DAS and even the theoretical value, the obtained resolution using the RC is clearly worsened with respect to the PSF method for each of the algorithms, with differences ranging from 50%–70% (MV-M/4, DMAS, CF) to 110%–130% (MV-M/2, MV-DMAS). The reason behind such an overestimation of the PSF method is attributed to the way these complex algorithms exploit the spatial and temporal coherence of the received signals. Mathematically, coherence is translated into weighting coefficients directly, as in MV or CF, or indirectly, through a combinatorial multiplication (DMAS). To illustrate this, lets consider the PSF of an image with a single point source. The maximum coherence will be found at its centre, being reduced as the reconstruction process shifts along pixels away from the centre within the main lobe of the PSF, resulting in an overall reduction of the signal amplitude at these pixels and, consequently, a reduction of the width of the PSF. Interestingly, when two point sources are considered using the RC method, their interaction is more complex, specially due to the presence of side-lobes, and advanced beamformers fail to resolve close targets, even at separation distances far above the lateral resolution determined by the single-source PSF method. The impact of the side-lobe interaction in the reconstruction using advanced beamformers is also observed in the axial resolution results of Fig. 7, where the side-lobe interaction is not present and the differences between the two methods are much reduced.

To illustrate the overestimation of the lateral resolution using advanced beamformers and the PSF criterion, reconstructed images and their corresponding horizontal profiles of two closely-spaced targets

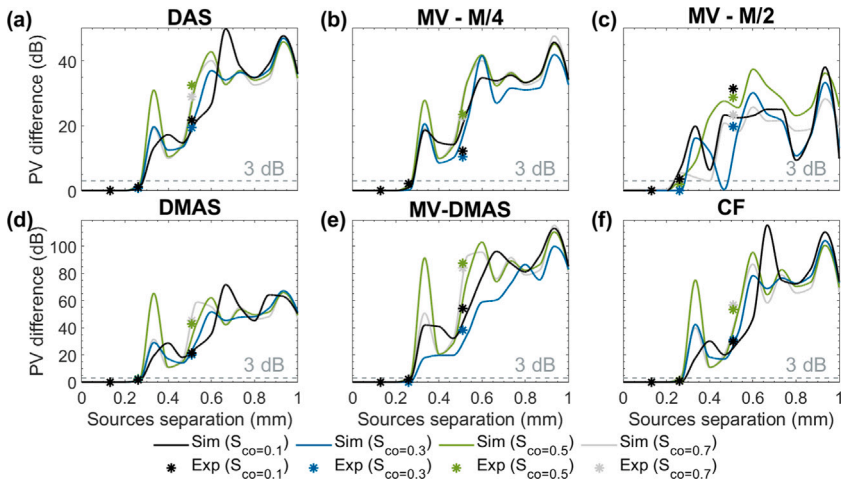


Fig. 5. Evolution of PV with the distance between sources on the axial axis. Results using the different algorithms implemented are represented from (a) to (f). The 3-dB threshold of the PV difference defining the RC axial resolution is plotted with a grey dashed line.

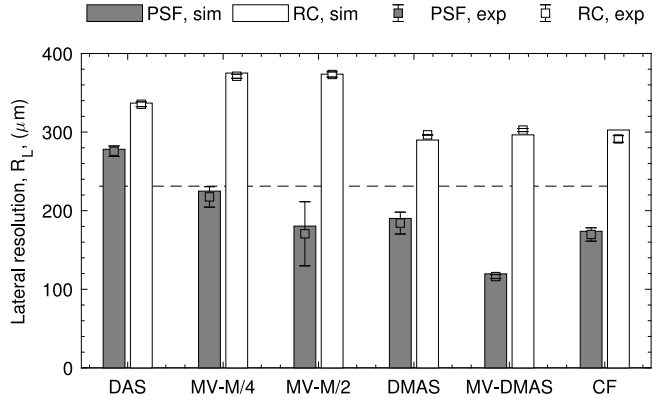


Fig. 6. Lateral resolution for each beamformer, calculated using the PSF method (grey) and RC (white), for simulation (bars) and experiments (markers). The theoretical resolution is indicated with a black dashed line.

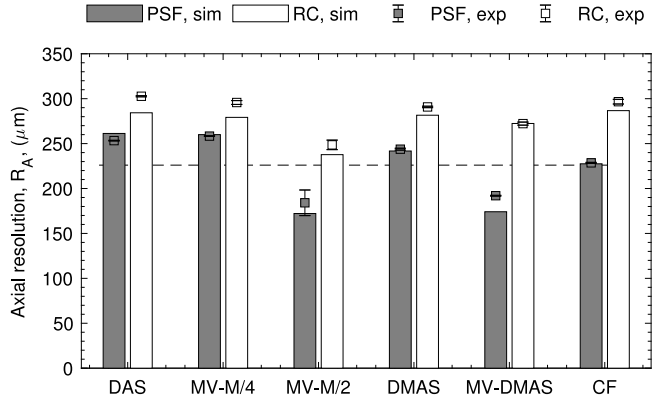


Fig. 7. Axial resolution for each beamformer, calculated using the PSF method (grey) and the RC (white), for simulations (bars) and experiments (markers). The theoretical resolution is indicated with a black dashed line.

using the standard DAS beamformer and several advanced beamformers are shown in Fig. 8. Critical sources separation distances have been chosen, at slightly above the resolution values given by each method, so that all targets should be properly resolved. First, for the reference case, the linear and non-adaptive DAS (Fig. 8(a)), although there is not much difference between the lateral resolutions given by the two methods,

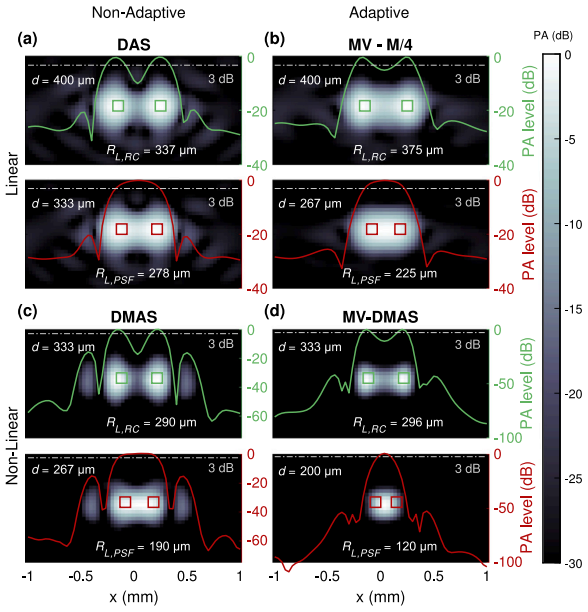


Fig. 8. PA images and horizontal profiles of two point targets separated at critical distances where the PSF and Rayleigh criterion indicate that they are resolved. (a) Reference linear and non-adaptive DAS. (b) linear and adaptive MV-M/4. (c) non-linear and non-adaptive DMAS. (c) non-linear and adaptive MV-DMAS. Horizontal profiles of the target central cross-section are shown: in green for resolved and in red for not resolved targets. White dashed lines indicate the 3-dB threshold. (For interpretation of the references to colour in this figure legend, the reader is referred to the web version of this article.)

for a separation distance of 333 μm, which is above the PSF resolution, the two sources are not resolved (red curve in Fig. 8(a)). However, at 400 μm sources separation, slightly above the RC resolution, they are fully distinguishable. If advanced beamformers MV, DMAS, MV-DMAS are considered, this gap is greatly magnified. As shown in Figs. 8(b), (c), (d), sources separated respectively by 267, 267 and 200 μm, should be resolved according to the PSF criterion. However, targets are not distinguished in the PA images, as indicated with the horizontal profiles shown in red, while the RC method correctly indicates that the sources are not resolved since their separation is below its resolution value. Also, in the case of clearly distinguishable sources, the RC method correctly indicates they are resolved, as shown from the green profiles in Fig. 8. Note that MV - M/2 and CF, not shown here, manifest a similar behaviour.

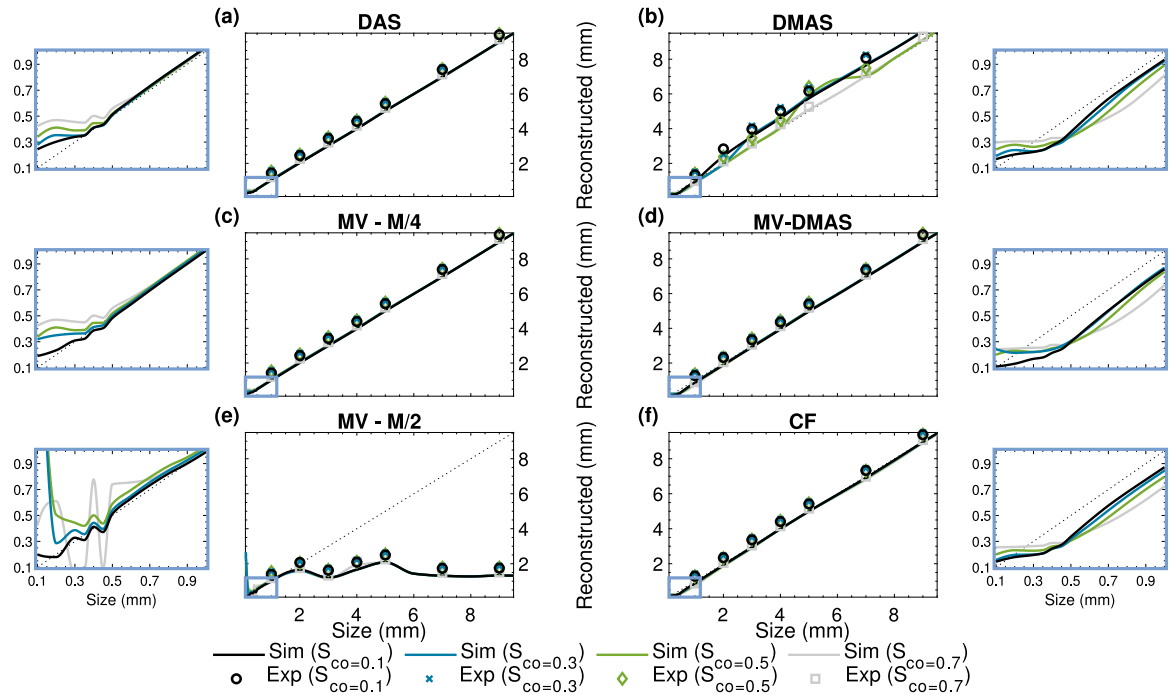


Fig. 9. Results of the source size accuracy study are represented from (a) to (f) for all the implemented beamformers. Black dashed lines represent the actual size of the sources. The insets on the left and right of the figure show in detail the 0 to 1 mm source sizes plot, where only the numerical study has been carried out.

3.2. Size evaluation

Fig. 9 shows the reconstructed sizes of square-shaped pieces of increasing size. As a reference, the actual size of the sources is represented by black dashed lines. Continuous lines indicate the reconstructed sizes using numerical simulations, according to the post-processing described in Section 2.2 and Fig. 3(b). The experimentally reconstructed sizes of 3D printed pieces are plotted using markers, and decreasing values of the sensitivity cut-off parameter are represented. A good agreement is obtained between simulations and experiments. Simulated sizes have been extended to smaller sources from 0.1 mm to 1 mm to consider sizes of the order of the PA system resolution, as shown in the insets on the left and right sides of Fig. 9.

As illustrated in Fig. 9 (a–d, f), reconstructed sizes have a good accuracy for PA sources larger than 1 mm, well above the system resolution (see Fig. 6). Nevertheless, the MV algorithm with $L = M/2$ reconstructs much smaller sources sizes than the actual ones well above the system resolution, both numerically and experimentally (see Fig. 9(e)). Although this beamformer accurately computes target positions, even for very small sources, it fails to properly evaluate their sizes, mainly due to the use of the maximum spatial window size, improving resolution at the expense of robustness.

The inset of Fig. 9(a) shows the numerical results for small sources using DAS. As expected, accuracy for under-resolution PA sources is poor, since reconstructed sizes are limited to the system resolution, while above the system resolution sizes are successfully represented following the reference line. MV beamformers using a DAS framework (insets in Fig. 9(c), (e)) also converge to the reference line at the system resolution, although the window size plays a relevant role. For a conservative window size (M/4), the trend for under-resolution targets is similar to DAS. On the contrary, for under-resolution targets using the largest window (M/2), results are not following a clear trend, the robustness of the method seems compromised and the obtained profiles are strongly affected by slight differences on the size of the pieces.

The remaining beamformers DMAS, MV-DMAS and CF, shown respectively in the insets of Fig. 9(b), (d) and (f), follow the same trend for under-resolution targets, converging to the system resolution, as expected. However, above the system resolution, these beamformers underestimate the reconstructed sizes remarkably, with errors ranging from 10% to 40% when evaluating pieces from 0.3 to 1 mm side. The reason behind this is a direct consequence of exploiting the spatial and temporal coherence of the received signals. When the source size is of the order of the resolution of the system, coherence varies gradually along the PSF of the target. Along the object, coherence is maximum, but at its edges the coherence is gradually reduced, resulting in a reduction of the overall signal amplitude and a subsequent reduction of the object size. Moreover, comparing these beamformers with MV based on DAS, the influence of the non-linearity coming from DMAS and the CF have a bigger impact on the size estimation than the one coming from the weights obtained by the covariance matrix estimation of MV. Note that the error on the size evaluation is reduced when decreasing the sensitivity cut-off parameter, although it exists along the whole range of analysed values.

4. Conclusions

In this work, an evaluation and analysis of two fundamental imaging characteristics of photoacoustic tomography systems using linear-array ultrasound probes has been carried out, incorporating advanced beamformers (including linear and non-linear, adaptive and non-adaptive). Attention has been brought to evaluate two main characteristics: (1) the suitability of using the PSF method to evaluate the spatial resolution of PAT systems using advanced beamforming algorithms; (2) an accuracy analysis of the reconstructed sizes of both under- and above-resolution targets.

To determine whether the PSF method is an appropriate tool to evaluate the spatial resolution, we have compared the lateral and axial resolutions obtained with this method to a methodology based on the Rayleigh criterion, where two point targets separated at increasing distances are considered, for which a numerical and experimental analysis has been carried out. As demonstrated throughout this work, the PSF method overestimates the lateral resolution when applying adaptive and/or non-linear beamformers, such as MV, DMAS, MV-DMAS and CF. While the obtained resolution values using the PSF method suggests

that two targets separated at a certain distance should be distinguished or resolved, PA images (and their corresponding profiles) of two point targets separated at larger distances than the PSF-resolution demonstrate that it is not the case. This aspect is particularly relevant as typical imaging scenarios in real tissues are generally complex, including multiple scatterers producing strong wave interactions, which makes the RC a more suitable resolution criterion than the PSF. It is also demonstrated that both methods differ on their spatial resolution by a 25%, following the analytical prediction shown in Fig. 1 when applying the DAS beamformer, which is only based on purely physical wave properties and not on advanced post-processing techniques that leverage the temporal and spatial coherence of the received signals.

To further analyse the implications of using advanced beamformers in the morphology fidelity of PA images, we imaged targets of multiple and previously known sizes, comparing them to their reconstructed sizes, using both classical and advanced beamformers. Results indicate that targets well above the resolution of the PAT system are reconstructed accurately, with the only exception of the MV beamformer for its maximum window size. However, when target sizes are close and slightly above the PAT system resolution, non-linear beamformers (DMAS, MV-DMAS) and the adaptive CF beamformer underestimate the actual target sizes, with errors ranging from 10% to 40% for PAT system used in this work.

These complex beamformers have recently become very popular in linear array-based systems due to their ability to mitigate the unwanted consequences of their narrow angular spectrum and limited aperture, which eventually leads to a poor spatial resolution and small areas of stable reconstruction. The results shown in this work shed light on the proper characterization of spatial resolution and target size determination of PAT systems encompassing advanced algorithms. This would be helpful, for instance, in the selection of advanced beamformers for medical practice where PA images of tumours and its surrounding vascularization are acquired to study their size and morphology evolution, especially if the PAT system resolution is near the physiological sizes of interest.

Declaration of competing interest

The authors declare the following financial interests/personal relationships which may be considered as potential competing interests: Noé Jiménez financial support was provided by Spanish Ministry of Science, Innovation and Universities. Alejandro Cebrecos reports financial support from Universitat Politècnica de València. Irene Pi financial support was provided by Generalitat Valenciana.

Data availability

Data will be made available on request.

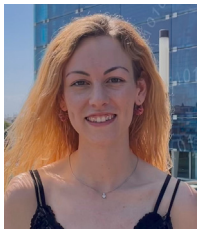
Acknowledgements

We are grateful for financial support from Agencia Estatal de Investigación (PID2019-111436RBC22 and PID2022-142719OB-C21), Generalitat Valenciana through the programs Equipamiento e Infraestructuras FEDER 2021-22 IDIFEDER/2021/004 and Programa de Garantía Juvenil I+D EDGJID/2021/189, and Agéncia Valenciana de la Innovació through Grant INNVA1/2022/50. N. Jiménez is grateful for financial support from the Spanish Ministry of Science, Innovation and Universities (MICIU) through grants "Juan de la Cierva - Incorporación", IJC2018-037897-I and "Ramón *y* Cajal" RYC2021-034920-I. A. Cebrecos is grateful for financial support from Universitat Politècnica de València through programs PAID-10-19 PAID-PD-22. Irene Pi is grateful for financial support from Generalitat Valenciana through programme CIACIF/2021/403.

References

[1] L.V. Wang, J. Yao, A practical guide to photoacoustic tomography in the life sciences, Nat. Methods 13 (2016) 627–638.
[2] Z. Chen, E. Rank, K.M. Meiburger, C. Sinz, A. Hodul, E. Zhang, E. Hoover, M. Minneman, J. Ensher, P.C. Beard, et al., Non-invasive multimodal optical coherence and photoacoustic tomography for human skin imaging, Sci. Rep. 7 (2017) 1–11.
[3] Y. Lao, D. Xing, S. Yang, L. Xiang, Noninvasive photoacoustic imaging of the developing vasculature during early tumor growth, Phys. Med. Biol. 53 (2008) 4203.
[4] M. Toi, Y. Asao, Y. Matsumoto, H. Sekiguchi, A. Yoshikawa, M. Takada, M. Kataoka, T. Endo, N. Kawaguchi-Sakita, M. Kawashima, et al., Visualization of tumor-related blood vessels in human breast by photoacoustic imaging system with a hemispherical detector array, Sci. Rep. 7 (2017) 1–11.
[5] X.-H. Zhang, D.-B. Cheng, L. Ji, H.-W. An, D. Wang, Z.-X. Yang, H. Chen, Z.-Y. Qiao, H. Wang, Photothermal-promoted morphology transformation in vivo monitored by photoacoustic imaging, Nano Lett. 20 (2020) 1286–1295.
[6] R.A. Kruger, R.B. Lam, D.R. Reinecke, S.P. De. Rio, R.P. Doyle, Photoacoustic angiography of the breast, Med. Phys. 37 (2010) 6096–6100.
[7] H. Estrada, A. Özbek, J. Robin, S. Shoham, D. Razansky, Spherical array system for high-precision transcranial ultrasound stimulation and optoacoustic imaging in rodents, IEEE Trans. Ultrason. Ferroelectr. Freq. Control 68 (2020) 107–115.
[8] M. Nasiriavanaki, J. Xia, H. Wan, A.Q. Bauer, J.P. Culver, L.V. Wang, High-resolution photoacoustic tomography of resting-state functional connectivity in the mouse brain, Proc. Natl. Acad. Sci. 111 (2014) 21–26.
[9] Y. Xu, L.V. Wang, G. Ambartsoumian, P. Kuchment, Reconstructions in limited-view thermoacoustic tomography, Med. Phys. 31 (2004) 724–733.
[10] K.S. Valluru, J.K. Willmann, Clinical photoacoustic imaging of cancer, Ultrasonography 35 (2016) 267.
[11] G.R. Kim, J. Kang, J.Y. Kwak, J.H. Chang, S.I. Kim, J.H. Youk, H.J. Moon, M.J. Kim, E.-K. Kim, Photoacoustic imaging of breast microcalcifications: A preliminary study with 8-gauge core-biopsied breast specimens, PLoS One 9 (2014) e105878.
[12] S.A. Ermilov, M.P. Fronheiser, H.-P. Brecht, R. Su, A. Conjusteau, K. Mehta, P. Otto, A.A. Oraevsky, Development of laser optoacoustic and ultrasonic imaging system for breast cancer utilizing handheld array probes, in: Photons Plus Ultrasound: Imaging and Sensing 2009, vol. 7177, SPIE, 2009, pp. 28–37.
[13] A. Garcia-Uribe, T.N. Erpelding, A. Krumholz, H. Ke, K. Maslov, C. Appleton, J.A. Margenthaler, L.V. Wang, Dual-modality photoacoustic and ultrasound imaging system for noninvasive sentinel lymph node detection in patients with breast cancer, Sci. Rep. 5 (2015) 1–8.
[14] T.N. Erpelding, A. Garcia-Uribe, A. Krumholz, H. Ke, K. Maslov, C. Appleton, J. Margenthaler, L.V. Wang, A dual-modality photoacoustic and ultrasound imaging system for noninvasive sentinel lymph node detection: Preliminary clinical results, in: Photons Plus Ultrasound: Imaging and Sensing 2014, vol. 8943, SPIE, 2014, pp. 792–797.
[15] J. Yao, L. Wang, Photoacoustic microscopy, Laser Photonics Rev. 7 (5) (2013) 758–778.
[16] B.E. Treeby, E.Z. Zhang, B.T. Cox, Photoacoustic tomography in absorbing acoustic media using time reversal, Inverse Problems 26 (2010) 115003.
[17] M. Xu, L.V. Wang, Universal back-projection algorithm for photoacoustic computed tomography, Phys. Rev. E 71 (2005) 016706.
[18] P. Burgholzer, J. Bauer-Marschallinger, H. Grün, M. Haltmeier, G. Paltauf, Temporal back-projection algorithms for photoacoustic tomography with integrating line detectors, Inverse Problems 23 (2007) S65.
[19] K.P. Köstli, P.C. Beard, Two-dimensional photoacoustic imaging by use of fourier-transform image reconstruction and a detector with an anisotropic response, Appl. Opt. 42 (2003) 1899–1908.
[20] B.T. Cox, P.C. Beard, Fast calculation of pulsed photoacoustic fields in fluids using k-space methods, J. Acoust. Soc. Am. 117 (2005) 3616–3627.
[21] T. Kirchner, F. Sattler, J. Gröhl, L. Maier-Hein, Signed real-time delay multiply and sum beamforming for multispectral photoacoustic imaging, J. Imaging 4 (2018) 121.
[22] B.M. Asl, A. Mahloojifar, Minimum variance beamforming combined with adaptive coherence weighting applied to medical ultrasound imaging, IEEE Trans. Ultrason. Ferroelectr. Freq. Control 56 (2009) 1923–1931.
[23] M. Mozaffarzadeh, A. Mahloojifar, M. Orooji, K. Kratkiewicz, S. Adabi, M. Nasiriavanaki, Linear-array photoacoustic imaging using minimum variance-based delay multiply and sum adaptive beamforming algorithm, J. Biomed. Opt. 23 (2018) 026002.
[24] K. Hollman, K. Rigby, M. O'donnell, Coherence factor of speckle from a multi-row probe, in: 1999 IEEE Ultrasonics Symposium. Proceedings. International Symposium (Cat. No. 99CH37027), vol. 2, IEEE, 1999, pp. 1257–1260.
[25] J. Camacho, M. Parrilla, C. Fritsch, Phase coherence imaging, IEEE Trans. Ultrasonics, Ferroelectr. Freq. Control 56 (2009) 958–974.
[26] H. Azhari, Basics of Biomedical Ultrasound for Engineers, John Wiley & Sons, 2010.
[27] O.M.H. Rindal, A. Rodriguez-Molares, A. Austeng, The dark region artifact in adaptive ultrasound beamforming, in: 2017 IEEE International Ultrasonics Symposium, IUS, IEEE, 2017, pp. 1–4.

[28] O.M.H. Rindal, A. Austeng, A. Rodriguez-Molares, Resolution measured as separability compared to full width half maximum for adaptive beamformers, in: 2020 IEEE International Ultrasonics Symposium, IUS, IEEE, 2020, pp. 1–4.
[29] J.W. Goodman, Introduction to Fourier Optics, Roberts and Company publishers, 2005.
[30] L.V. Wang, S. Hu, Photoacoustic tomography: In vivo imaging from organelles to organs, Science 335 (2012) 1458–1462.
[31] R.J. Thomas, B.A. Rockwell, W.J. Marshall, R.C. Aldrich, S.A. Zimmerman, R.J. Rockwel. Jr., A procedure for multiple-pulse maximum permissible exposure determination under the z136. 1-2000 American National standard for safe use of lasers, J. Laser Appl. 13 (2001) 134–140.
[32] B.E. Treeby, B.T. Cox, K-wave: Matlab toolbox for the simulation and reconstruction of photoacoustic wave fields, J. Biomed. Opt. 15 (2010) 021314.
[33] V. Perrot, M. Polichetti, F. Varray, D. Garcia, So you think you can das? A viewpoint on delay-and-sum beamforming, Ultrasonics 111 (2021) 106309.
[34] G. Matrone, A.S. Savoia, G. Caliano, G. Magenes, Ultrasound synthetic aperture focusing with the delay multiply and sum beamforming algorithm, in: 2015 37th Annual International Conference of the IEEE Engineering in Medicine and Biology Society, EMBC, IEEE, 2015, pp. 137–140.
[35] S. Jeon, E.-Y. Park, W. Choi, R. Managuli, K. jong Lee, C. Kim, Real-time delay-multiply-and-sum beamforming with coherence factor for in vivo clinical photoacoustic imaging of humans, Photoacoustics 15 (2019) 100136.
[36] P. Stoica, R.L. Moses, et al., Spectral Analysis of Signals, Vol. 452, Pearson Prentice Hall Upper Saddle River, NJ, 2005.



Irene Pi-Martín B.Sc. in Biomedical Engineering from Universitat Politècnica de València (2020) and M.Sc. specializing in Diagnostic and Therapeutic Devices from the same institution (2021). She is currently a Ph.D. candidate at the Instituto de Instrumentación para Imagen Molecular (I3M), a hybrid scientific research institute belonging to Spanish National Research Council (CSIC) and Universitat Politècnica de València. Her doctoral research focuses on novel techniques and applications of molecular imaging using photoacoustics.



Alejandro Cebrecos B.Sc. in Telecommunication, Sound and Image (2009), M.Sc. in Acoustics (2010) and Ph.D. by the Universitat Politècnica de València (2015). Post-doctoral researcher at the Spanish Instituto de Instrumentación para Imagen Molecular (I3M, CSIC). His research is devoted to advanced ultrasound biomedical imaging, particularly to Photoacoustic imaging systems, but he is also interested in the field of phononic crystals and acoustic metamaterials, both in the audible and ultrasonic regimes. He was visiting scholar for 1 year at the University of Colorado at Boulder during 2014, and a post-doc for 3 years at the French CNRS Laboratoire d'Acoustique de l'Université du Mans. He has published 20 journal papers and participated in more than 60 conferences.



Juan J. García-Garrigós Ph.D. in Electronic Engineering from Universitat Politècnica de València (2013), M.Sc. in Electronic Engineering, M.Sc. in Artificial Intelligence and B.Sc. in Theoretical Physics from Universitat de València. He is a post-doctoral researcher at Instituto de Instrumentación para Imagen Molecular (I3M, CSIC-UPV) since 2015. He worked as R&D engineer on biometric systems for the company Fermax Electrónica until 2006. He made his thesis on beam instrumentation for next generation lepton colliders (CLIC) in the Instituto de Física Corpuscular (IFIC, Valencia) and CERN (Geneva, Switzerland). He was project associate researcher at CERN in the Beams department for the LHC until 2014. His research interest currently is focused on biomedical laser applications and photoacoustic imaging.



Noé Jiménez He received the B.Sc. degree in telecommunication and the M.Sc. and Ph.D. degrees in acoustics from the Universitat Politècnica de València, Valencia, Spain, in 2007, 2010, and 2015, respectively. In 2014 and 2019, he worked for the European Space Agency, Paris, France, for noise control at the launch pad using periodic structures. In 2015, he joined the French CNRS (UMR6613), Paris, for a postdoctoral position to research on deep-subwavelength acoustic metamaterials. In 2017, he enrolled Spanish National Research Council (CSIC) to research on biomedical ultrasound applications with the Instituto de Instrumentación para Imagen Molecular (I3M), Valencia. He has been a Visiting Researcher with Columbia University, New York City, NY, USA Université du Mans, Le Mans, France, and with the University of Salford, Manchester, U.K. Since 2013, he has published more than 43 journal articles and participated in more than 150 conferences. He holds five patents. His research interests concern from fundamental research in waves in complex and structured media to biomedical ultrasound applications.



Francisco Camarena He holds a Ph.D. in Physics at Universitat de València. He is Associate Professor in the Applied Physics Department at Universitat Politècnica de València. He develops ultrasound-based techniques for both medical and industrial applications. In 2016 founded and currently directs the Ultrasound Medical and Industrial Laboratory at Institute of Instrumentation for Molecular Imaging (I3M), supervising 3 postdoctoral researchers, 7 Ph.D. students and several undergraduate students. He is the director of the IVIO-UPV Chair and the coordinator of the Scientific Unit of Business Innovation at I3M. He has published 60 articles in peer-reviewed journals and has participated in 27 national and international R&D projects funded in public calls, 11 as principal investigator in the last 10 years.